The Innovative Application of Gravity Data Inversion and Geophysical Edge-Detection for Celestine Exploration: A Case Study at the Siraf Mine, Semnan Province, Iran

Seyed Hossein Hosseini [a] , Ahmad Afshar [b, *] , Nastaran Ostadmahdi Aragh [c]

[a] *Institute of Geophysics, University of Tehran, Tehran, Iran.*

[a] *Faculty of Mining Engineering, Amirkabir University of Technology, Tehran, Iran.*

[a] *School of Mining Engineering, College of Engineering, University of Tehran, Tehran, Iran.*

ABSTRACT

This study represents a pioneering application of gravimetric methods for the exploration of celestine mineralization. Through the inversion of gravity data, we identified areas with significant density variations indicative of potential mineral deposits, particularly those with high celestine content. Utilizing depth estimation techniques such, as Euler deconvolution and MNTHD and MNTDR filters, we accurately delineated the boundaries and depths of anomalies, generally within 5 meters of the surface, with specific validation in celestine-rich regions. The three-dimensional model derived from data inversion indicates that large-scale mineralization is improbable. However, with a density cutoff of 1 g/cm³, the potential for several small veins is apparent. Due to the inherent non-uniqueness and ambiguity in geophysical modelling, the precise assessments of reserves and ore grades will require systematic exploratory drilling. The gravity prospect maps and three-dimensional density model have partially detected the anomalies with practical constraints, such as challenging topography and disturbed geological conditions impacting further measurements. To advance exploration, we recommend specific drilling coordinates and additional geophysical surveys with a 5-meter grid spacing, contingent on favourable initial drilling results. This study underscores the effectiveness of gravimetric methods in identifying celestine mineralization and suggests that these techniques may enhance exploration strategies and methodologies.

Keywords: *MNTHD, MNTDR, Gravity method, Celestine deposit exploration, 3D inverse modelling.*

1. Introduction

Celestine, a mineral composed of strontium sulfate ($SrSo_4$) is the most important economic mineral of strontium. Celestine is the primary raw material used to produce strontium chemicals for applications in ceramics, glass, red pyrotechnics, and metallurgy [1]. In 1997, the estimated global production of celestine (strontium sulfate) was 0.306 million tons with a value of $72 per ton. Currently, celestine is mined in seven countries with the principal producers being Mexico, Spain, Turkey, and Iran [2]. The most common exploration methods for celestine deposits are geological studies (e.g., tectonics, field studies, stratigraphic observations, sampling, mineralogy) and geochemical exploration methods [3-5]. Geophysical techniques have not been extensively employed or are not currently considered a primary method for the exploration of celestine deposits.

Geophysical exploration methods entail the measurement of subsurface rock properties using various techniques, aimed at discovering and prospecting for concealed resources (such as oil, gas, water, and economically valuable minerals) within the Earth's depths, as well as geotechnical applications. In geophysical studies, various physical parameters of the Earth, such as gravity, magnetic field, electrical resistivity, seismic wave behavior, self-potential, electromagnetic polarization, and more are measured and investigated. Each of these geophysical parameters is measured by special methods

[6,7]. Among the methods mentioned above, gravity surveys have been successfully applied in a wide range of mineral exploration projects [8-14] and have also proven effective in geothermal exploration [15,16]. Certain dense metallic ores and mineral deposits can create distinctive gravity anomalies, variations in the Earth's gravitational field. These gravity anomalies can be detected by conducting gravity surveys. Analyzing the data from these gravity surveys allows geologists to identify potential areas of mineralization where valuable mineral deposits may be located. Sadraeifar and Abedi (2024) conducted a ground-gravity survey to investigate the Ghare-Aghaj potash resource, which has a low-density contrast with surrounding rocks. Their research successfully identified the deposit boundaries and pinpointed the prospect area. The results were in good agreement with well data and indicated the distribution of salt with vertical expansion below the surface [14]. Layade, et al. (2021) used Gravity survey to investigate the subsurface by measuring the differences in the Earth's gravitational field. They employed the methods of the filtering techniques as well as forward and inverse modelling for data analysis and interpretations. The findings indicate that the density contrasts in gravitational formations imply the existence of mineral compositions, such as limestone, quartz, gneiss, sandstone, schist, granite, quartzite, and gypsum [11]. Afshar et al. (2018) investigated the feasibility of using potential field data,

---

including magnetic and gravity surveys, for the geophysical exploration of sodium sulfate (salt-cake) resources. More specifically, the focus is on the minerals Glauberite (sodium sulfate) and Eugsterite (sodium calcium sulfate), which are two prevalent minerals found in the Garmab mine located in Semnan province, Iran [9]. Yang and Li (2023) focused on using gravity and aeromagnetic data to delineate deep, concealed ore-controlling structures in the Qingchengzi ore field [13]. Gravity data were used to evaluate the depth and thickness of geothermal resources, revealing significant geothermal anomalies. Additionally, gravity data along with magnetic and magnetotelluric methods were employed by Afshar et al. (2023) to develop a detailed geological model of the Sabalan geothermal area, identifying key features, such as faults and hydrothermal reservoirs. Both studies underscored the effectiveness of integrating gravity data with other geophysical methods in geothermal resource exploration [15, 16].

This research has carried out gravity studies in the Siraf area. Due to the existence of celestine outcrops in the mentioned mining area, gravity surveys were conducted to further explore and examine potential celestine mineralization. The most significant point of this study is the detection of the non-metallic mineral celestine by gravity surveys due to the high density of celestine (3.95 g/cm^3). Although gravity methods are cost-effective and widely used geophysical methods in mineral exploration, the application of these methods for celestine deposit exploration is not well documented within the literature. This study aims to address this gap by focusing on the investigation of gravity methods within this particular area of interest. Notably, this study leverages the high-density characteristics of celestine to enhance the efficacy of geophysical exploration methods.
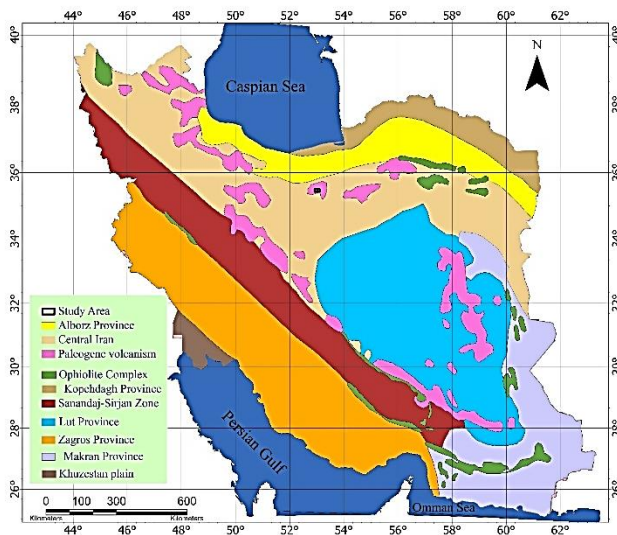
Fig. 1. The location of the study area on the structural geology map of Iran.

2. Geological Setting

2.1. Regional Geology

As shown in Fig. 1, the studied area is situated to the south of the Alborz structural zone and north of the Central Iran structural zone, specifically within the Paleogene volcanic region. The Eocene deposits (equivalent to the Karaj and Kund Formation) are the oldest outcrops in the Sarvak Formation. In the area spanning the southern parts of the Alborz Zone and the boundary with Central Iran, the geological formations present include the Lower Red, Upper Red, and to a certain degree, the Qom Formation. During the Oligo-Miocene, equivalent to the Pyrenean phase, the Eocene and older deposits were folded and uplifted, resulting in a marine transgression and the initiation of the deposition of the Qom Formation, upon which calcareous and marly

sediments were been formed. The second identifiable tectonic event, correlative with the Passadenian phase, resulted in the gentle folding of conglomeratic sedimentary rocks.

The significant and influential fault in the Sarvak Formation is the Alborz Thrust Fault, which has a left-lateral component and a west-east trend, and is approximately aligned with the Eocene deposits (mountain and plain boundary). Other faults are generally observed as lineaments, especially in the Miocene deposits. A limited number of small strike-slip faults with north-south or northwest-southeast trends are present in the central (Qaravol anticline) and southwestern areas, and are located on the Lower and Upper Red formations.

This region contains a mix of small and moderately large anticlines and synclines, primarily shaped by compressional forces and occasionally influenced by subsurface salt domes. One notable feature is the small Qaravol anticline, characterized by a core of the Lower Red Formation and trending in an east-west direction, situated in the northern section of the area. The Qom and Upper Red formations constitute the southern and northern limbs of this anticline.

2.2. Local Geology

The study area is located on the 1:100,000 geological map of the Sorkheh, which was produced and published by the Geological Survey and Mineral Exploration Organization. In Fig. 2, the position of the area on the 1:100,000 map of the Sorkheh is depicted. Relying on this map and field investigations, the rock units within the study area are predominantly composed of shale, siltstone with intercalated gypsum layers, tuff, and lithic tuff.
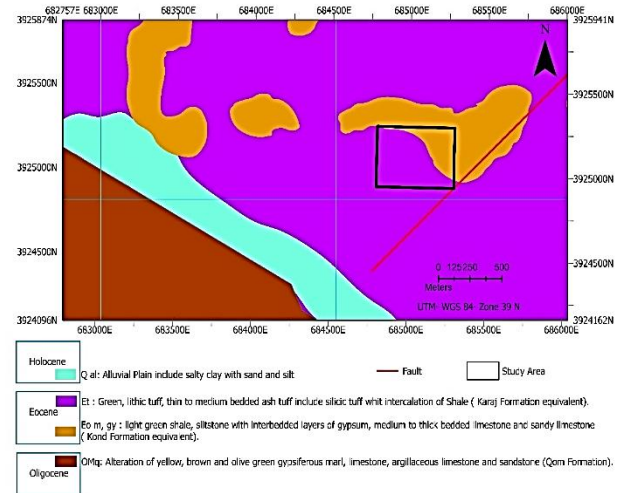
Fig. 2. The geological map of the studied area (reproduced from the Sorkheh 1:100,000 geological map)

2.2.1. Stratigraphic units

EO^{m,gy} unit: This geological unit is composed of marl, clay, and siltstone shales with interbedded layers of gypsum and occasionally fossiliferous limestone and calcareous sandstone. The color varies from light green to light gray to pinkish. The gypsum layers consist of masses with interbeds and numerous lenses of limestone. The limestone rocks are often crystalline and porous. This unit, found in the northern part of the Sorkheh Formation, has undergone deformation due to dome-like movements, forming gypsum masses, taking on a chaotic appearance and cutting across adjacent formations.

E^t unit: This unit is also exposed in the northern and northwestern parts of the Sarvak Formation and consists of thin to medium-bedded, light greenish-gray tuff. The tuff layers include siliceous tuffs, calcareous tuffs, lithic tuffs, and crystalline tuffs with a medium-acidic composition, along with interbedded shale layers that exhibit good bedding and range

in color from green to light cream. The thickness of this unit reaches approximately 500 to 800 meters, and it may be equivalent to the Karaj Formation.

In general, the 1:100,000 scale Sorkheh map consists of three geomorphological units: semi-elevated mountainous areas, hills, and low-lying plains. The study area is located in the northwest of the Sorkheh map, comprising semi-elevated mountainous sections. These semi-mountainous regions include greenish volcanic tuffs, greenish-colored clastic deposits, shale, and gypsum outcrops. Fig. 3 shows the topographic map derived from elevation measurements at the geophysical survey stations using multi-frequency GPS. At the gravity survey measurement locations, the minimum recorded elevation is 1480 meters, the maximum recorded elevation is 1650 meters, and the average elevation of the area is 1550 meters above sea level.

2.3. Ore genesis

Celestine (strontium sulfate) deposits are formed through several significant geological processes:

Direct Precipitation: Celestine forms directly from solution when Sr2+-rich fluids mix with sulfate-rich fluids, causing the strontium sulfate to precipitate.

Replacement: Sr2+-rich fluids replace gypsum or carbonate minerals, resulting in the formation of celestine or strontianite ($SrCO_3$). Celestine deposits often exhibit evidence of replacing pre-existing gypsum or carbonate layers. The Sr in these fluids typically originates from the dissolution of Sr-bearing minerals in the host rocks.

Early Diagenesis: Celestine forms through the early diagenetic replacement of gypsified stromatolites, resulting in large orebodies. This process has been documented in certain deposits, such as those found in Montevive, Spain.

These geological processes are crucial for the formation of celestine deposits, which are typically associated with marine carbonate and evaporite sequences [5, 17,18].

2.4. Economic Geology

This area exhibits the presence of several non-metallic mineral deposits, including halite (common salt), gypsum, sulfur, and sodium carbonate.

Rock salt: In salt diapirs, rock salt outcrops, and on the map, it is observed as a salt dome within the Lower Red units in the form of a dyke-like structure. Gypsum and marl overlie the rock salt as cap rocks, and considering the extent of salt diapir outcrops and rock salt, a negligible reserve of this mineral resource may exist in this area.

Gypsum: This mineral resource is present in substantial quantities within the Sarvak Formation. Occasionally, the gypsum exhibits a high degree of purity, and the individual gypsum beds can be quite thick. The occurrences of gypsum are noted in the Eocene sedimentary sequence, as well as within the Lower and Upper Red formations.

Celestin and Barite: As previously noted, the sedimentary sequence of the study area's syncline includes the Karaj, Semnan, and Kund Formations, with celestine being widespread in the lower layers of the Kund Formation. The Kund Formation consists mainly of gypsum, limestone, and calcareous sandstone, deposited in an evaporitic setting. Based on the fossils found in the limestone layers of this sequence, it dates back to the Upper Eocene period and was deposited in a shallow evaporitic basin characterized by fluctuating and gradual subsidence. The layer-like celestine, rhythmic, and elongated lenses parallel to the overall sedimentary layering of the region, formed during the early and main stages of diagenesis. Field investigations reveal that celestine crystals exhibit two distinct morphologies: a) elongated, well-formed to irregularly-shaped fragments, and b) lenticular crystals that mimic the pseudomorphic shape of gypsum. Silicification, a late-stage diagenetic process, has preferentially altered the celestine-bearing layers to a greater extent compared to the surrounding non-celestine layers. Field investigations reveal that celestine crystals exhibit two distinct morphologies: a) elongated, well-formed to irregularly-shaped fragments, and b) lenticular crystals that mimic the pseudomorphic

shape of gypsum. Silicification, a late-stage diagenetic process, has preferentially altered the celestine-bearing layers to a greater extent compared to the surrounding non-celestine layers. Considering the form and mode of occurrence of celestine within the evaporitic sequence, the genesis of its major portion is predominantly diagenetic, while a minor part of it was likely formed simultaneously with sedimentation due to the saturation of strontium-rich solutions in the evaporitic environment. It appears that due to the abundance of gypsum in the shallow evaporitic environment and consequently the high concentration of sulfate ions in the water, as well as the lower solubility of strontium sulfate compared to calcium sulfate, the presence of strontium ions in the environment led to the formation of strontium sulfate (celestine). Furthermore, as a result of the migration of strontium ions from the lower layers (Semnan and Karaj Formations) towards the Kund Formation or their displacement by fluid flow during diagenetic stages, it is possible for celestine to replace gypsum. The relatively higher concentration of strontium ions in the Karaj and Semnan Formations increases the likelihood of sourcing these ions from the mentioned formations. With this description, the high potential for the possible mineralization of celestine has become the main factor defining the current gravity survey studies [19].

In this region, celestine mineralization appears as layered, rhythmic, and elongated lenses that run parallel to the sedimentary layers. This formation took place during the early and primary stages of diagenesis. Celestine crystals manifest in two forms: elongated, well-formed crystals and lens-shaped crystals, sometimes resembling gypsum. Silicification, occurring during the later stages of diagenesis, has notably affected the celestine-bearing layers more than other layers. The majority of celestine formation based on its shape and distribution is predominantly evaluated as diagenetic within the evaporitic sequence. However, a minor portion may have formed due to strontium saturation in the evaporitic environment, concurrently with sediment deposition. Given the prevalence of gypsum in shallow evaporitic environments and the associated high sulfate ion concentration, coupled with the lower solubility of strontium sulfate compared to calcium sulfate, the presence of strontium ions apparently facilitated the formation of strontium sulfate (celestine). Additionally, the migration of strontium ions from underlying formations (Semnan and Karaj) towards the Kund Formation or their replacement by atmospheric fluid flows during diagenetic stages, may have led to the replacement of gypsum by celestine. The relatively high concentration of strontium ions in the Karaj and Semnan Formations suggests a probable contribution of these formations to the strontium supply. Examples of celestine and gypsum crystals from the study area are presented in Figs. 4.a and 4.b.

3. Materials and methods

3.1. Inversion methodology

Numerous sophisticated algorithms have been developed for the inversion of geophysical data. Among them, Li and Oldenburg (1996) introduced a comprehensive algorithm that has become one of the most widely adopted and esteemed methods in the domain of geophysical data inversion. The objective function proposed by Li and Oldenburg is formulated as follows [20]:

$$\varphi(m) = \varphi_d(m) + \beta\varphi_m(m) \tag{1}$$

In this context, $\varphi_d(m)$ represents the misfit function, β stands for the regularization parameter, and $\varphi_m(m)$ denotes the model norm. The misfit function is formulated as follows:

$$\varphi_d = \|W_d(Gm - d^{obs})\|_2^2 \tag{2}$$

Where $d^{obs} = [d_1 \, d_2 \, d_3 \, ... \, d_N]^T$ represents the vector of potential field data, while G denotes the forward operator matrix with dimensions N×M, which is computed using the mathematical formulations of forward modelling. The vector $m = [m_1 \, m_2 \, m_3 \, ... \, m_M]^T$ corresponds to the model parameter set, and $W_d = diag[1/\sigma_1 \, ... \, 1/\sigma_n]$ is the data weighting matrix, where σ_i signifies the standard deviations (uncertainties) associated with the i-th datum. In this context, φ_d is a

$\chi^2{}_N$ variable with N degrees of freedom, implying that minimizing the misfit function will yield an acceptable solution or response for modelling purposes [20].

Since the number of model parameters exceeds the number of data points (M≫N), the problem is ill-posed and requires assumptions about the model to solve the non-uniqueness. Therefore, the model norm in the continuous case is defined as follows [20-21]:

$$\varphi_m(m) = \alpha_s \int_V w_s [w_r(z)(m-m_0)]^2 \, dV + \alpha_x \int_V w_x \left[\frac{\partial}{\partial x}\big(w_r(z)(m-m_0)\big)\right]^2 dV + \alpha_y \int_V w_y \left[\frac{\partial}{\partial y}\big(w_r(z)(m-m_0)\big)\right]^2 dV + \alpha_z \int_V w_z \left[\frac{\partial}{\partial z}\big(w_r(z)(m-m_0)\big)\right]^2 dV \quad (3)$$

In this expression, m_0 represents the initial or reference geological model, α_s is the coefficient controlling the similarity of the solution to the initial model, α_x ' α_y ' α_z are coefficients controlling the smoothness, w_s, w_x, w_y, w_z are the weighting functions, and V denotes the modelling space. Additionally, preventing the model from retrieving undesired depths, w_r (z) is also defined as:

$$w_r(z) = \big(z_j + z_0\big)^{-\vartheta/2} \quad (4)$$

Here, z_j denotes the depth to the center of a cell, while z_0 is an adjustable parameter obtained by fitting the function w_r (z), which represents the field generated at an observation point by a column of cells. The parameter ϑ is adjusted based on the attenuation of the potential field. Generally, for gravity data, a value of $\vartheta = 2$ is recommended. However, for a more precise determination of ϑ, the structural index of gravity anomalies can also be used as a reference [20, 21].
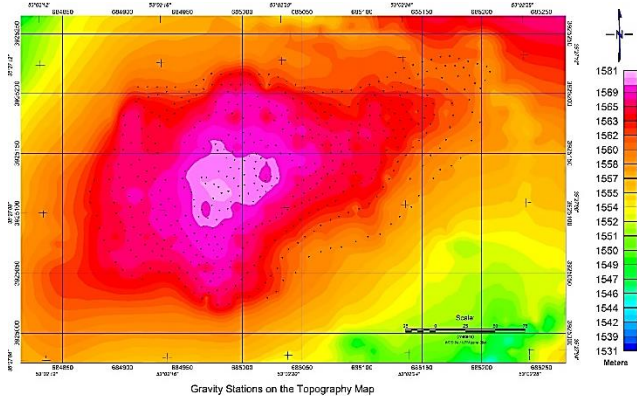
Fig.3. Gravity stations overlaid on the elevation map, represented by black dots indicating the survey locations.
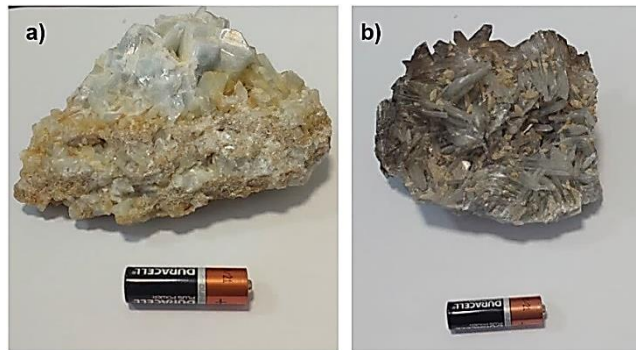
Fig.4. a) The image displays a celestine crystal, with a battery used as the scale reference. b) Acicular gypsum crystals discovered in proximity to the celestine mineralization outcrops.

3.2. Edge detection and depth estimation methods

3.2.1. Euler Depth Estimation Method

The Euler deconvolution technique is extensively applied in the automated analysis of potential field data (gravity) in both three-dimensional and two-dimensional formats. Through this approach, one can accurately determine the position and depth of geological formations responsible for gravity irregularities on two-dimensional maps. The conventional representation of the Euler method adheres to equation 2:

$$(x - x_0)\frac{\partial f}{\partial x} + (y - y_0)\frac{\partial f}{\partial y} + (z - z_0)\frac{\partial f}{\partial z} = N(B - f) \quad (5)$$

Where $(x_0. y_0. z_0)$ represents the position of the potential field source (f) that was measured at the station (x, y, z). B represents the background value of the potential field, while N denotes the structural index, which signifies the shape of the anomaly source. The values of N for various shapes are provided in Table 1. To determine the depth and position of an anomaly source by solving the Euler equation, a moving window approach is employed to select the relevant data. For each window location, a set of linear equations is resolved using the least squares technique [22-26].

Table 1. Structural Index (S.I.) values for Euler depth estimation.

Structure	sphere or dipole	cylinder	dyke ،sill	Contact
S.I gravity data	2	1	0	-1

3.2.2. Edge detection technique

This study employed the methods developed by Ghiasi et al. in 2023 to accurately identify the edges of magnetic anomalies. In summary, the MNTHD filter combines horizontal (THD) and vertical (d^2f/dz^2) derivatives of potential field data, thereby minimizing false edges and improving the resolution of the edge boundaries.

The MNTHD equation is presented below:

$$MNTHD = \tan^{-1}\left(\frac{THD \times \frac{min(\partial^2 f/\partial z^2)}{max(\partial^3 f/\partial z^3)}}{\left|\frac{\partial^2 f}{\partial z^2}\right| + p \times \max\left[THD \times \frac{min(\partial^2 f/\partial z^2)}{max(\partial^3 f/\partial z^3)}\right]}\right) \quad (6)$$

Here, f represents the total potential field data, THD denotes the Total Horizontal Derivative, and p is an adjustable parameter ranging from 0 to 0.5. The maximum MNTHD values signify the edges of the potential anomalies field [27, 28].

The MNTDR edge detection filter, an enhanced version of the THDR filter, incorporates multiple horizontal and vertical derivatives in its formula. As a result, the MNTDR filter produces narrower edges and more detailed results, although it can sometimes be more susceptible to noise and false edges compared to the MNTHD. The MNTDR equation is given by:

$$MNTDR = \tan^{-1}\left(\frac{THDR \times \frac{min(\partial^2 f/\partial z^2)}{max(\partial^3 f/\partial z^3)}}{\left|\frac{\partial^2 f}{\partial z^2}\right| + p \times \max\left[THDR \times \frac{min(\partial^2 f/\partial z^2)}{max(\partial^3 f/\partial z^3)}\right]}\right) \quad (7)$$

In this equation, f signifies the total potential field data, THDR indicates the Total Horizontal Derivatives of the tilt angle filter [29], and p serves as an adjustable parameter that ranges from 0 to 0.5, which should be determined by the interpreter. The maximum MNTDR filter values correspond to the edges of the potential anomaly field.

A comparison of the filters reveals that the MNTHD filter produces smoother edges with more hollows due to the mathematical functions used in its formula, whereas the MNTDR method yields narrower perimeters with relatively more noise. By considering the geological units of the study area and applying both filtering techniques in conjunction with 3D inversion methods, a comprehensive view of the surface projection of deep and large-scale anomalies can be obtained [27, 28].

3.3. Analytical signal

Enhancing details in data and identifying the edges of target bodies, the analytical signal is a valuable tool in potential field geophysical methods. This technique involves applying the Hilbert transform to the original data, which separates the real and imaginary parts of the signal. The analytical signal is particularly effective in recognizing edges or boundaries of subsurface structures by emphasizing changes in the signal. It is often used in combination with other methods, such as Euler deconvolution, to provide a more comprehensive understanding of the subsurface structure. The analytical signal approach has been successfully applied in various geophysical contexts, including mineral exploration, to delineate subsurface structures. By highlighting the edges of anomalies, the analytical signal map can help identify the boundaries of potential mineral deposits or other geological features of interest [30, 31].

3.4. Gravity data

Gravity measurements were collected using a SCINTREX CG3-M gravimeter over the area. Due to rough topographic conditions and execution difficulties, these gravity data were acquired along several scattered profiles, with station spacing ranging from 5 to 10 meters. The area of interest was covered by a total of 600 gravity stations.

The gravity data were corrected for instrumental drift, free-air, terrain, tides, and Bouguer effects. A density of 2.55 g/cm³ was used to produce the Bouguer anomaly map, which is suitable for sedimentary basins [30-31] and was chosen based on Nettleton's method [33]. Fig. 5 shows the Bouguer anomaly map of the study area, with gravity values ranging from -0.228 to 0.666 mGal. This anomaly map displays several short- and long-wavelength anomalies caused by shallow and deep (residual and regional) sources, respectively.

There are several methods for regional-residual anomaly separation [32]. In this study, we implemented an optimized filtering method known as the preferential continuation method, introduced by Guo et al. (2013), to reduce the effects of regional anomalies and enhance the near-surface desired sources (Figs. 6 and 7) [34].

4. Data interpretation in the studied area

In mineral exploration, gravimetric studies focus on identifying regions with varying densities compared to surrounding areas within the study site. To accomplish this, it is essential to quantify and isolate the individual impacts of all forces influencing the device. This process, referred to as gravimetric corrections, needs to be computed individually for each station. Through the elimination of disruptive forces and the addition of required forces to the recorded measurements at each station (measured in mGal), the changes in gravitational force resulting from variations in the density of geological structures within the area are ascertained. Prior to conducting gravity surveys, it is crucial to have a geological map of the area at a suitable scale. Furthermore, geophysical operations can assist in resolving ambiguities in geological and mineral issues in subsurface layers that are not readily apparent to geologists at the surface (Such as buried faults beneath alluvium, the distribution of subsurface mineral deposits and others) [32, 36,37].

The amplitude of analytical signal and Tilt Derivative maps, derived from combining the horizontal and vertical derivative maps, are shown in Figs. 8 and 9. Generally, these maps provide a better delineation of the boundaries of anomalies compared to previous maps, with their values reaching a maximum at the center of the anomalies. The maximum values of the MNTHD and MNTDR filters indicate the edges of the anomalies, and for thin vein anomalies, these filters can also highlight their centers. As shown in Figs. 10 and 11, these filters effectively delineate the anomalous areas and their alignment with the location of the outcrops confirms this observation.

The Euler deconvolution method was employed to estimate the depth of anomaly sources. Given that the celestine mineralization is vein-like, the depths were estimated by assuming a dyke structure and setting SI=0 in Table 1. The results are depicted as colored circles on the residual

gravity anomaly map (Fig. 12). As shown in this map, the estimated depth of the sources is less than 5 meters in the anomaly areas, and these findings are supported by observations from outcrops and trenches.

4.1. 3D inverse modeling

The 3D modelling of gravity data was performed using the UBC-Grav3d package, developed by the University of British Columbia in Canada, which operates based on the Li-Oldenburg inversion method [38]. For this purpose, the residual anomaly data were considered as input for the inversion program. Then, the subsurface space up to an elevation of 450 meters was discretized into 10-meter cubic cells, and by performing the inversion calculations, the density value of each cubic cell was obtained. In Fig. 14, a three-dimensional view of the discretized mesh used for inversion is shown along with the residual anomaly. The inversion calculations were performed for each cell of the model, and the density of each cell was obtained.
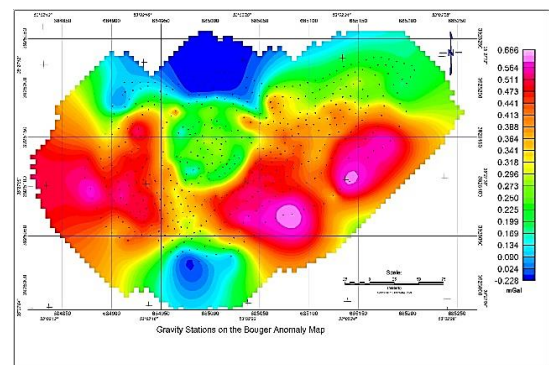
Fig. 5. Gravity Station on the Bouguer Anomaly Map. The black dots show the gravity stations
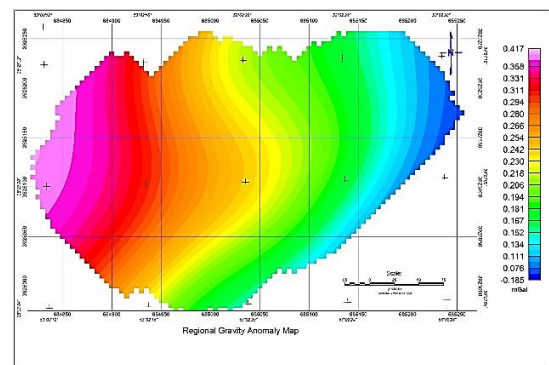
Fig. 6. Regional Gravity Anomaly Map.
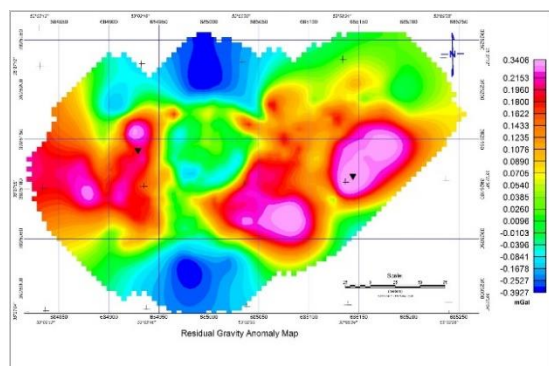
Fig. 7. Residual Gravity Anomaly Map. Black inverted triangles indicate the location of the celestine outcrops. anomalies with high intensity values can be areas prone to celestine mineralization.

In potential field data interpretation (gravity and magnetic), upward continuation maps can be used to qualitatively assess the depth extension of anomalies. For this purpose, upward continuation filters were applied at heights ranging from 10 to 50 meters, with an interval of 10 meters. The results, along with the residual anomaly map, are presented in a three-dimensional view in Fig. 13. As shown in this figure, the anomaly pattern almost disappears in the 30-meter upward continuation map, indicating a depth extent of approximately 30 meters for the bottom of the anomaly sources.
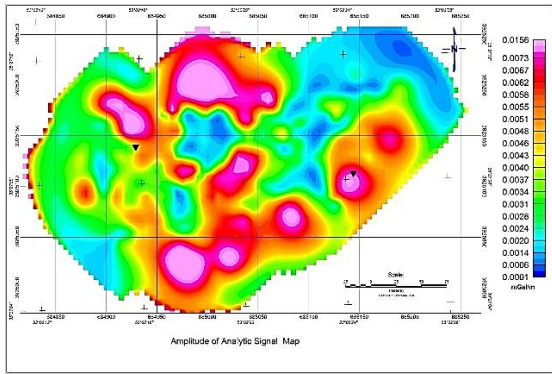
Fig. 8. Amplitude of Analytical Signal map. Black inverted triangles indicate the location of the celestine outcrop.
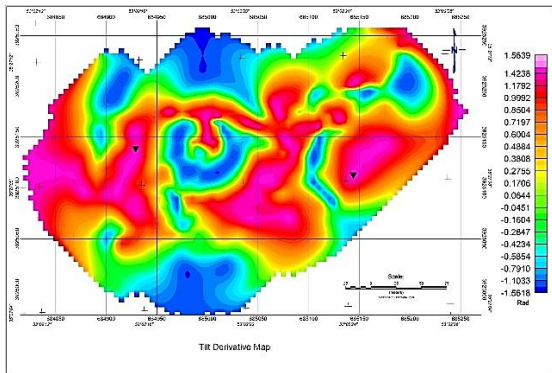
Fig. 9. Tilt Derivative Map. The Black inverted triangles indicate the location of the celestine outcrop.
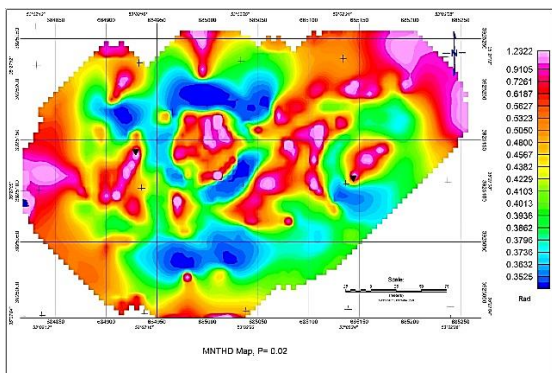
Fig. 10. MNTHD filter with P= 0.02. The Black inverted triangles indicate the location of the celestine outcrop.

Fig. 15 presents the results of the inverse modelling using both vertical and horizontal sections. The three-dimensional density model is illustrated with vertical sections at X=684930 m, X=685140 m, and Y=3925130 m, and a horizontal section at Z=1510 m. Panel a provides a view from the top and southeast, while Panel b shows the view from the

top and southwest. This visualization offers insight into the spatial distribution and depth variations of the modeled density anomalies. Areas with high density values can be interpreted as potential regions for celestine mineralization.
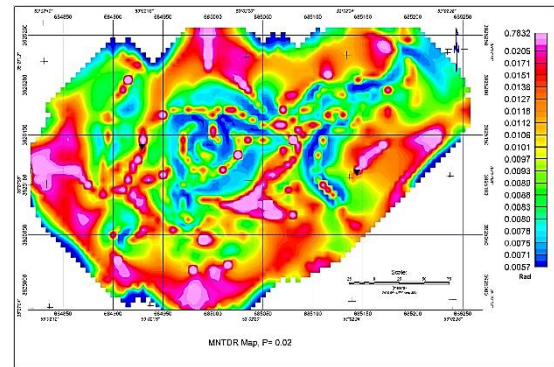
Fig. 11. MNTDR filter with P= 0.02. The Black inverted triangles indicate the location of the celestine outcrop.
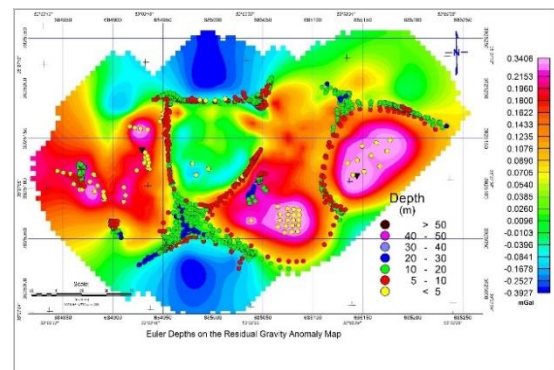
Fig. 12. The results of depth estimation by the Euler deconvolution method using a window of 50 meters and a structural coefficient equal to zero.
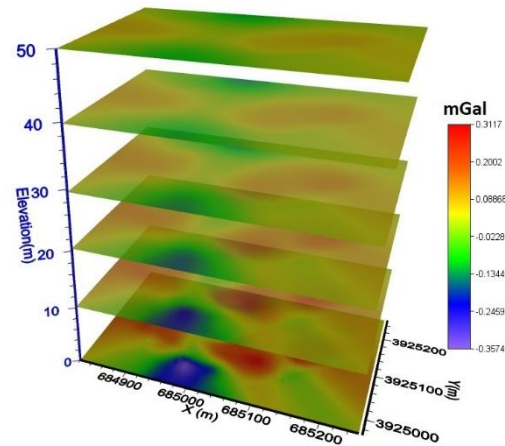
Fig. 13. Upward Continuation map at heights of 10 to 50 meters with 10-meter intervals over the gravity residual anomaly map.

5. Conclusion

- The analysis of gravity data reveals significant variations in gravity values across the study area. Bouguer anomaly maps show substantial gravity fluctuations ranging from -0.228 to 0.666 mGal. These variations are attributed to both regional and residual sources. Optimized filtering methods were employed to separate these anomalies, thereby enhancing the detection of near-surface features.

Fig. 14. Subsurface space discretization for 3D inverse modeling procedure.
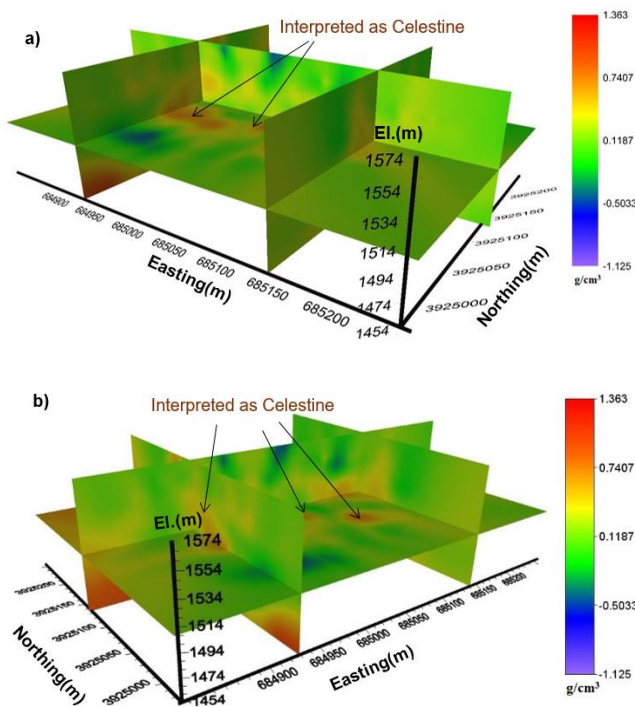
Fig. 15. A view of the three-dimensional density model using vertical sections at X=684930 m, X=685140 m and Y=3925130 m and horizontal section Z=1510 m. a) View from top and southeast. b) View from top and southwest

- The simulation and modelling of gravity data using advanced algorithms have identified areas with significant density variations relative to their surroundings. High gravity anomaly regions, potentially indicative of mineral deposits, are clearly evident in the modeled maps. The results demonstrate the effective simulation of mineral-rich areas, particularly those with high celestine content.

- Depth estimation methods, including Euler deconvolution as well as MNTHD and MNTDR filters, have accurately estimated the boundaries and potential depths of anomaly sources. The results of the Euler method suggest that the depth of anomaly sources is generally less than 5 meters with validation particularly evident in areas where celestine features are observed. The three-dimensional model derived from data inversion indicates that large-scale mineralization is improbable. However, with a density cutoff of 1 g/cm³, the model suggests the potential presence of several small veins. The accuracy of weight and density estimates from the model is affected by inherent non-uniqueness and ambiguity in geophysical data modelling. Precise reserve and ore grade determination will require systematic exploratory drilling, especially given the similarity

in specific gravity between celestine and barite, which complicates differentiation using these geophysical methods.

- Gravity prospect maps and the three-dimensional density model reveal only a partial manifestation of the anomaly. Difficult topography, disturbed geological conditions, and steeply inclined mine walls rendered further measurements in these areas impractical. To advance exploration efforts, recommended coordinates for exploratory drilling are provided in Table 2 and illustrated on the residual anomaly map in Fig. 15. If drilling results and geological studies yield positive findings, additional geophysical surveys with a dense 5-meter grid spacing are recommended.

- Further analysis and comparison with available field data confirm a good agreement with the modeled results. Analytical signal techniques and anomaly filtering have facilitated more precise delineation and identification of anomaly edges. The final results are particularly validated in regions with the presence of celestine and other mineral deposits. These findings highlight that gravity methods, especially considering the high-density features of celestine, can be effective tools for discovering and identifying mineral resources in similar areas. The results may contribute to the development of new exploration techniques and the optimization of existing methods.

- Field observations and the review of geophysical maps with mineral outcrops suggest that the broad extent of anomalies relative to the mineral deposits may be due to the relatively wide spacing of data collection points. It is recommended to conduct a more detailed exploration with a denser survey grid, ideally with 5-meter by 5-meter spacing for improved accuracy in mineral identification.

Acknowledgement

References

[1] Ober, J. A., (1997), Strontium. US Geol Survey Minerals Inf Circ, 6 p.

[2] Hanor, J. S. (2000). Barite–celestine geochemistry and environments of formation. Reviews in Mineralogy and Geochemistry, 40(1), 193-275.

[3] Tekin, E. (2001). Stratigraphy, geochemistry and depositional environment of the celestine-bearing gypsiferous formations of the Tertiary Ulaş-Sivas Basin, East-Central Anatolia (Turkey). Turkish Journal of Earth Sciences, 10(1), 35-49.

[4] González-Sánchez, F., Camprubí, A., González-Partida, E., Puente-Solís, R., Canet, C., Centeno-García, E., & Atudorei, V. (2009). Regional stratigraphy and distribution of epigenetic stratabound celestine, fluorite, barite and Pb–Zn deposits in the MVT province of northeastern Mexico. Mineralium Deposita, 44, 343-361.

[5] Zhu, Q., Cook, N. J., Xie, G., Ciobanu, C. L., Gilbert, S. E., Wade, B., & Xu, J. (2022). Textural and geochemical analysis of celestine and sulfides constrain Sr-(Pb-Zn) mineralization in the Shizilishan deposit, eastern China. Ore Geology Reviews, 144, 104814.

[6] Hosseini, S. H., Habibian Dehkordi, B., Abedi, M., & Oskooi, B. (2021). Implications for a geothermal reservoir at Abgarm, Mahallat, Iran: Magnetic and magnetotelluric signatures. Natural Resources Research, 30, 259-272.

[7] Talebi, M. A., Hosseini, S. H., Abedi, M., & Moradzadeh, A. (2023). 3D inverse modeling of electrical resistivity and chargeability data through unstructured meshing, a case study for travertine exploration. International Journal of Mining and Geo-Engineering, 57(2), 131-140.

[8] Lyatsky, H. (2010). Magnetic and gravity methods in mineral exploration: The value of well-rounded geophysical skills. Recorder (Canadian Society of Exploration Geophysics), 30-35.

[9] Afshar, A., Norouzi, G. H., Moradzadeh, A., & Riahi, M. A. (2018). Application of magnetic and gravity methods to the exploration of sodium sulfate deposits, case study: Garmab mine, Semnan, Iran. Journal of Applied Geophysics, 159, 586-596.

[10] Essa, K. S., & Munschy, M. (2019). Gravity data interpretation using the particle swarm optimisation method with application to mineral exploration. Journal of Earth System Science, 128, 1-16.

[11] Layade, G. O., Edunjobi, H. O., Makinde, V., & Bada, B. S. (2021). Application of Forward and Inverse Modelling to High-Resolution Gravity Data for Mineral Exploration. Journal of the Earth and Space Physics, 46(4).

[12] Dubey, C. P., & Roy, A. (2023). Joint inversion of gravity and gravity gradient and its application to mineral exploration. J. Ind. Geophys. Union, 27(1), 1-18.

[13] Yang, Y., & Li, Y. (2023). Ore-controlling structures of the Qingchengzi Pb-Zn-Au-Ag orefield, northeastern China and significance for deep ore prospecting: Revealed from gravity and magnetic anomalies. Ore Geology Reviews, 156, 105376.

[14] Sadraeifar, B., & Abedi, M. (2024). 3D inversion of gravity data using mixed Lp–Lq norm regularization, a case study for potash targeting at the Ghare-Aghaj deposit in Iran. Carbonates and Evaporites, 39(3), 66.

[15] Afshar, A., Norouzi, G. H., Moradzadeh, A., Riahi, M. A., & Porkhial, S. (2017). Curie point depth, geothermal gradient and heat-flow estimation and geothermal anomaly exploration from integrated analysis of aeromagnetic and gravity data on the Sabalan Area, NW Iran. Pure and Applied Geophysics, 174, 1133-1152.

[16] Afshar, A., Norouzi, G. H., & Moradzadeh, A. (2023). Exploring Geothermal Potential through Multi-Modal Geophysical Data Integration: Gravity, Magnetic, and Magnetotelluric Prospecting. International Journal of Mining and Geo-Engineering, 57(4), 427-434. doi: 10.22059/ijmge.2023.364057.595093.

[17] Ariza-Rodríguez, N., Rodríguez-Navarro, A. B., Calero de Hoces, M., Martin, J. M., & Muñoz-Batista, M. J. (2022). Chemical and mineralogical characterization of montevive celestine mineral. Minerals, 12(10), 1261.

[18] Gao, Y., Sun, Y., Wang, D., Chen, B., & Gu, W. (2023). Geological and Geochemical Constraints on the Origin of the Sr Mineralization in Huayingshan Ore District, Chongqing, South China. Minerals, 13(2), 279.

[19] Aghanabati, S. A. (2013). Geology of Iran and neighboring countries. Geological Survey of Iran, 710.

[20] Li, Y., & Oldenburg, D. W. (1996). 3-D inversion of magnetic data. Geophysics, 61(2), 394-408.

[21] Ghanbarifar, S., Ghiasi, S. M., Hosseini, S. H., Abedi, M., Oskooi, B., & Smirnov, M. Y. (2024). Geoelectrical image of the Sabalan geothermal reservoir from magnetotelluric studies. Journal of Applied Geophysics, 224, 105359.

[22] Ghanbarifar, S., Hosseini, S. H., Abedi, M., & Afshar, A. (2024). A dynamic window-based Euler depth estimation algorithm for potential field geophysical data.

[23] Ghanbarifar, S., Hosseini, S. H., Ghiasi, S. M., Abedi, M., & Afshar, A. (2023). Joint Euler deconvolution for depth estimation of potential field magnetic and gravity data. International Journal of Mining and Geo-Engineering.

[24] Huang, L., Zhang, H.L., Li, C.F. et al. (2022). Ratio-Euler deconvolution and its applications. Geophysical Prospecting, 70, 1016–1032. https://doi.org/10.1111/1365-2478.13160

[25] Salem, A., & Ravat, D. (2003). A combined analytic signal and Euler method (AN-EUL) for automatic interpretation of magnetic data. Geophysics, 68, 1952–1961. https://doi.org/10.1190/1.1635379

[26] Thompson, D. T. (1982). EULDPH: A new technique for making computer-assisted depth estimates from magnetic data. Geophysics, 47(1), 31-37.

[27] Ghiasi, S. M., Hosseini, S. H., Afshar, A., & Abedi, M. (2023). A novel magnetic interpretational perspective on Charmaleh iron deposit through improved edge detection techniques and 3D inversion approaches. Natural Resources Research, 32(1), 147-170.

[28] Hosseini, S. H., Oskooi, B., Ghanbarifar, S., Ghiasi, S. M., Abedi, M., & Smirnov, M. Y. (2024). 2D sharp boundary inversion to determine tectonic and geological features of geothermal fields through the magnetotelluric method: case study of the Mahallat reservoir in Iran. Bulletin of Geophysics and Oceanography.

[29] Miller, H. G., & Singh, V. (1994). Potential field tilt—a new concept for location of potential field sources. Journal of applied Geophysics, 32(2-3), 213-217.

[30] Luo, Y., Wang, M., Luo, F., & Tian, S. (2011). Direct Analytic Signal Interpretation of Potential Field Data Using 2-D Hilbert Transform. Chinese Journal of Geophysics, 54(4), 551-559.

[31] Salem, A., Ravat, D., Gamey, T. J., & Ushijima, K. (2002). Analytic signal approach and its applicability in environmental magnetic investigations. Journal of Applied Geophysics, 49(4), 231-244.

[32] Hinze, W. J., von Frese, R. R., & Saad, A. H. (2013). Gravity and magnetic exploration: Principles, practices, and applications. Cambridge University Press.

[33] Jimenez-Munt, I., Fernandez, M., Saura, E., Vergés, J., & García-Castellanos, D. (2012). 3-D lithospheric structure and regional/residual Bouguer anomalies in the Arabia—Eurasia collision (Iran). Geophysical Journal International, 190(3), 1311-1324.

[34] Nettleton, L. L. (1939). Determination of density for reduction of gravimeter observations. Geophysics, 4(3), 176-183.

[35] Guo, L., Meng, X., Chen, Z., Li, S., & Zheng, Y. (2013). Preferential filtering for gravity anomaly separation. Computers & Geosciences, 51, 247-254.

[36] Blakely, R. J. (1996). Potential theory in gravity and magnetic applications. Cambridge University Press.

[37] Telford, W. M., Geldart, L. P., & Sheriff, R. E. (1990). Applied geophysics (Vol. 1). Cambridge university press. This classic textbook provides a comprehensive overview of gravimetry and other geophysical methods.

[38] UBC Geophysical Inversion Facility. (2005). GRAV3D Manual: A Program Library for Forward Modelling and Inversion of Gravity Data over 3D Structures. University of British Columbia